Applied Surface Science 546 (2021) 149076

Contents lists available at ScienceDirect

Applied Surface Science

journal homepage: www.elsevier.com/locate/apsusc

Full Length Article

Growth of out-of-plane standing $MoTe_{2(1-x)}Se_{2x}/MoSe_2$ composite flake films by sol–gel nucleation of MoO_y and isothermal closed space telluro-selenization

A. Fernández García [a], V. Torres-Costa [a], O. de Melo [a,b], F. Agulló-Rueda [c], G.R. Castro [c,d], M. Manso Silvan [a,e,*]

[a] Departamento de Física Aplicada and Instituto de Ciencia de Materiales Nicolás Cabrera, Universidad Autónoma de Madrid, Madrid, Spain
[b] Physics Faculty, University of Havana, Cuba
[c] Instituto de Ciencia de Materiales de Madrid (ICMM), Consejo Superior de Investigaciones Científicas (CSIC), 28049 Madrid, Spain
[d] SpLine, Spanish CRG BM25 Beamline at the ESRF, F-38000 Grenoble, France
[e] Centro de Microanálisis de Materiales, Universidad Autónoma de Madrid, 28049 Madrid, Spain

ARTICLE INFO

Keywords:
Sol–gel
Transition metal oxides
Transition metal dichalcogenides
Isothermal closed space vapour transport
Out-of-plane growth

ABSTRACT

This study describes the sol–gel processing of MoO_y on Si (1 0 0) to subsequently achieve out-of-plane $MoTe_2/MoSe_2$ flake composite films by an isothermal closed space vapor transformation. The oxide precursor films have been prepared from a Mo isopropoxide solution in isopropanol and acid catalysis induced by HCl. Thermal annealing at 200, 400 and 600 °C enhanced the condensation after xerogel formation. An x-ray absorption analysis demonstrates that films condensed at 200 °C are at an intermediate chemical state between MoO_3 and MoO_2. To achieve $MoTe_2/MoSe_2$ composite films, the precursor oxide films were reduced in H_2 and exposed to the chalcogenides by isothermal closed space vapor transport at 600 °C. The multilayered nanocomposite films grow with an out-of-plane flake-like structure and an evident integration of Se in the $MoTe_2$ phase according to a $MoTe_{2(1-x)}Se_{2x}$ alloy, with an estimation of x of 0.25. The alloy and the orientation of the flakes are consistent with the bands present in the Raman spectrum. These films are attractive for applications requiring high surface area interfaces favoring gas or ion exchange reactions with transition metal dichalcogenides.

1. Introduction

Monolayer and few-layered 2D materials are attracting a great attention recently due to their outstanding electronic properties, which give rise to a panorama of new applications in the fields of electronic [1,2], optical [2,3], chemical [4–6] and biomedical [7,8] devices. Among the different families of 2D materials, transition metal dichalcogenides (TMDs) are in advance in the confirmation of new interrelated properties and exhibit quantum spin Hall effect [9], band gap opening phase transformations [10] and tuneable magnetotransport [11], to cite a few. Especially attractive fundamental properties stem from the innovative ways to engineer the band gap structure, giving rise to strongly bound [12,13] and interlayer excitons [14], and additional phenomena contributing to valley optoelectronics [15,16]. Additionally, topological insulation has been theoretically predicted in TMD structures, although not yet confirmed experimentally [17].

Although most of these properties are exhibited by monolayer structures, TMDs tend naturally to form multi-layers [18] and heterostructures [19] rather than extended single or patch islands. This phenomenon has pushed research towards the modification of these Van der Waals materials by different techniques like elemental [20] or molecular intercalation [21] or strain engineering [22] that allow activating specific electrical conductivity and excitonic properties.

From the point of view of the processing of supported TMDs, there is a huge demand for protocols responding to the specific constraints of i.e. electrode derived applications. Although in-plane processing has been a fundamental step towards the confirmation of the solid-state properties of TMDs, a new input towards applications calls for the processing of porous [23] and out-of-plane TMDs [24]. In out of plane configurations, TMDs exhibit roughness and high surface area along with a strong

* Corresponding author at: Departamento de Física Aplicada and Instituto de Ciencia de Materiales Nicolás Cabrera, Universidad Autónoma de Madrid, 28049 Madrid, Spain.
E-mail address: miguel.manso@uam.es (M. Manso Silvan).

https://doi.org/10.1016/j.apsusc.2021.149076
Received 15 November 2020; Received in revised form 13 January 2021; Accepted 15 January 2021
Available online 19 January 2021

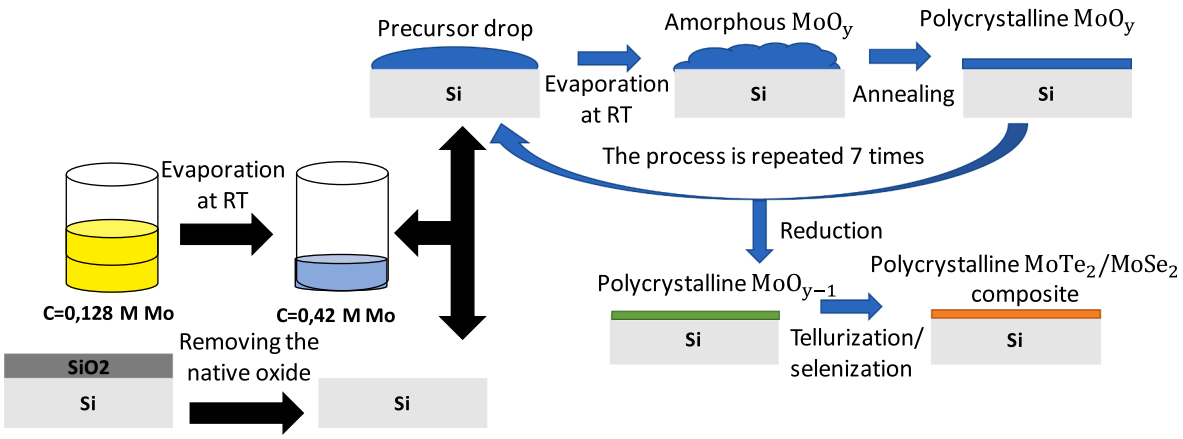

Fig. 1. Preparation and synthesis of $MoTe_2/MoSe_2$ composite films via reduction and tellurization/selenization of MoO_3 grown by drop-casting sol–gel method.

bonding to the surface, which is achieved through boundary atoms in the 2D material plane and the substrate. This latter feature adds complexity to the properties since the monolayers/multilayers acquire an interface induced asymmetry. These, and other kinds of porous TMDs are key in applications calling for ion or gas exchange, as in many catalytic, energy storage or sensing applications [25,26].

Relevantly, conventional SiO_2/Si substrates have been described as an ideal support for the growth of vertically oriented flake-like TMDs [27]. This interface is especially attractive due to its ease of interconnection with Si electronics that would enormously facilitate the transfer of technology to industry. The processing of vertically oriented TMDs has been thus the focus of different gas phase studies using chemical vapour deposition (CVD) [28], sputtering [29], hybrid ALD/CVD [30] and sequential plasma processes [31]. With respect to wet routes, a huge progress has been done using the sol–gel process to adapt the synthesis of TMD precipitates [32] to the direct deposition of large surface homogeneous films [33]. The most recurrent wet alternative is electrodeposition, although in this case the process is not direct and requires reduction and substitution post-processing [34] or implies the previous synthesis and functionalization of the TMDs [35].

In the current work, we focus on demonstrating the feasibility of out-of-plane ordered TMDs by a hybrid wet-gas phase process. We rely on the sol–gel process for the low temperature nucleation of MoO_y compounds over wafer-scale areas of a precursor transition metal oxide on silicon substrates [36] using molybdenum alkoxides [37]. We then post process the oxide through thermally activated reduction and isothermal closed-space vapour transformation, a technique previously used for the formation of TMDs from precursor transition metal oxide films [18]. We further aim at describing the microstructural and compositional changes through XRD, Raman Spectroscopy and SEM, which can explore the obtained surfaces after annealing from low temperature (200 °C) up to 600 °C in the search of the out-of-plane ordered TMD films. We concentrate on $MoTe_2/MoSe_2$ composites with a fixed processing stoichiometry as a proof of concept of the processability of TMD films with intermediate properties between $MoTe_2$ and $MoSe_2$ [38].

2. Experimental methods

2.1. MoO_y film preparation

The MoO_y precursor sol was prepared using molybdenum (V) isopropoxide ($Mo[OCH(CH_3)_2]_5$, 99.5% metal basis), to 5% w/v in isopropanol (Alfa Aesar), with pH = 1.3 regulated by using fuming hydrochloric acid 37% (HCl, Merck). The prepared solution was evaporated at room temperature for 48 h, to obtain a Mo concentration of 0.42 M. Before the deposition, the native oxide of the (1 0 0) Si wafer was removed with a piranha solution bath at room temperature. The solution and substrate preparation parts are illustrated in the bottom left part of Fig. 1. A precursor drop of 12 µL was deposited onto the activated (1 0 0) Si surface and left to dry at room temperature. Finally, samples were annealed in open air for 5 min at three different temperatures. The annealing temperature determined the deposited film label according to the following rule: MoOxT, with T being the annealing temperature value (200, 400 or 600) expressed in °C. The whole process drop-casting/evaporation/annealing was repeated 7 times (see the top left cycle, Fig. 1) to produce conformal flaky films.

2.2. MoO_2 and $MoTe_{2(1-x)}Se_{2x}$ film preparation

The nucleated structures produced by sol–gel drop casting were subsequently reduced at atmospheric pressure in H_2:Ar atmosphere at the same temperature as the first 5 min annealing but for 2 h, which eventually allowed achieving MoO_2 films according to the reaction [18]:

$$MoO_3(s) + H_2(g) \rightarrow MoO_2(s) + H_2O(g)$$

For the isothermal closed space vapour (ICSV) tellurization-selenization, a graphite boat with a solid mix of Te:Se equal to 8:2 was used. The sample annealed at 600 °C with a reducing gas mixture composed of H_2:Ar at 3:2 was exposed to the Te/Se source for 15 min at atmospheric pressure [18]. The ICSV process is illustrated in the bottom right part of Fig. 1.

2.3. Characterization of the samples

A structural analysis was performed using a Field Emission Scanning Electron Microscope (FESEM) Philips XL30 S-FEG and X-ray diffraction (XRD) with a Panalytical diffractometer X'Pert PRO (Θ/2Θ geometry, Cu anode and no monochromatic (K_α) radiation). Ellipsometry was used to analyse the precursor MoO_y films through comparison with reference optical properties using a J.A. Woolman Co. Inc. M-2000FI ellipsometer and EC-400 electronics. To determine the structural properties of the MoO_y nucleated at low temperature, an X-ray absorption (XAS) measurement in fluorescence configuration was performed in the CRG BM25A SpLine beamline of the *European Synchrotron Radiation Facility* (ESRF), which is equipped with a double Si (1 1 1) crystal monochromator. RBS was used to determinate the in-depth relative concentration of Mo, Te and Se. The incident ions were ^4_2He with an energy of 4.3 MeV collected at a scattering angle of 70°, which provides conditions for the determination of C traces. For the simulation of the spectra, we used SIMNRA software [39] with calculations using the resonant cross section provided by SigmaCalc 2.0.

Raman spectra were obtained with a Renishaw Ramascope 2000 spectrometer and an Argon ion laser emitting at a wavelength of 514.5 nm. The laser power was maintained low to avoid sample damage. A

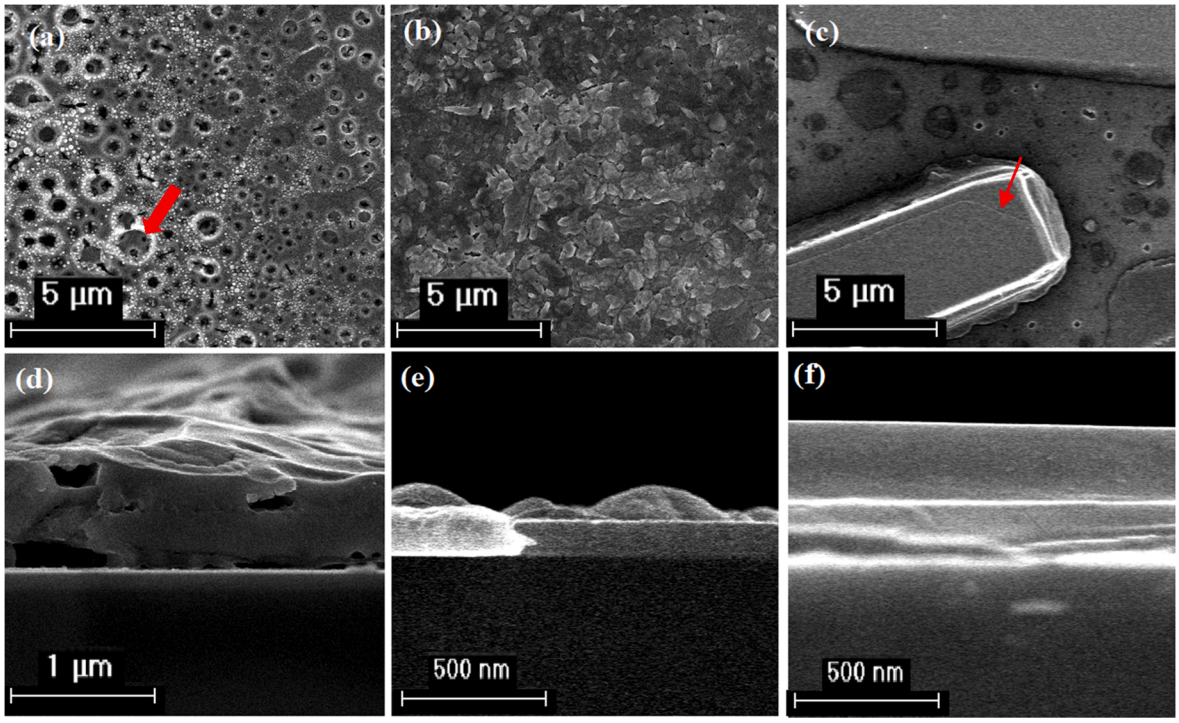

Fig. 2. a), b) and c) SEM images of the surface for the samples after annealing at 200, 400 and 600 °C; respectively. d), e) and f) cross section SEM images for the same samples, respectively.

metallographic optical microscope Olympus BH-2 was used to focus the laser light on the film and to collect the light scattered by the sample in a backscattering geometry. The optical axis was perpendicular to the sample surface. Several points of the sample were probed to check the homogeneity of the film.

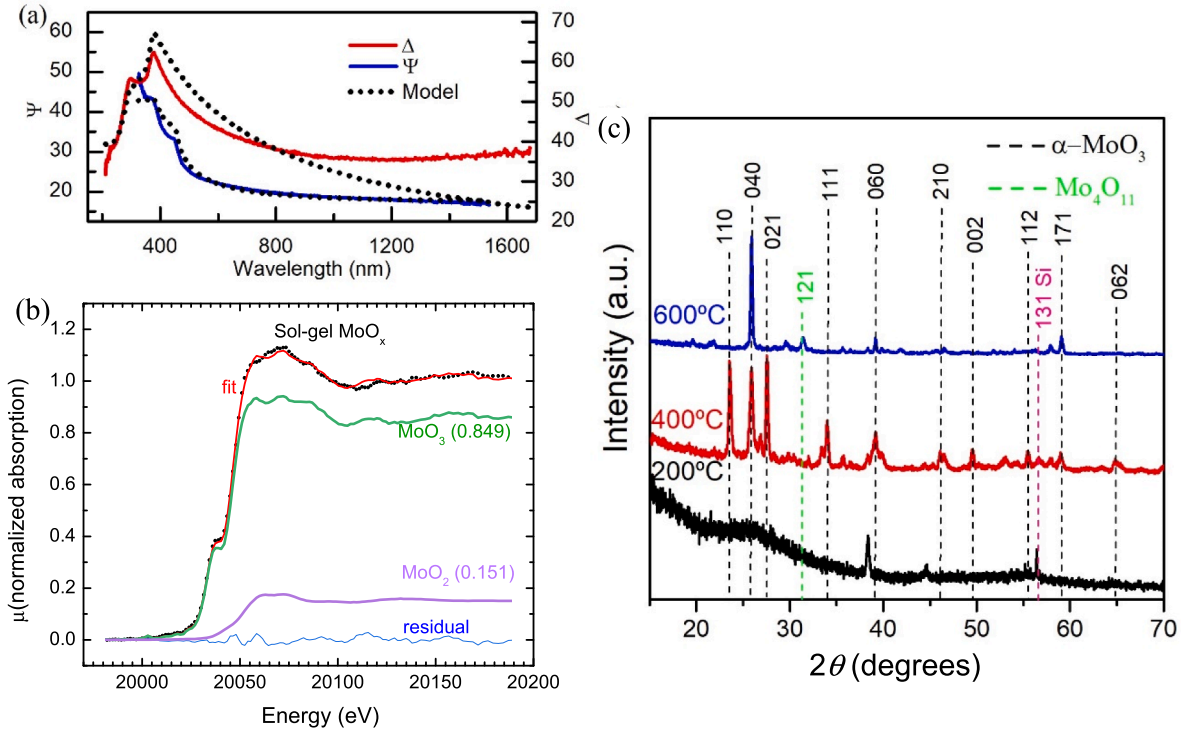

Fig. 3. (a) ψ and Δ dependence with light wavelength as derived from ellipsometry for the $MoO_y/SiO_2/Si$ stack produced by sol–gel drop-casting after annealing at 600 °C. (b) XAS spectrum at the molybdenum K edge from the MoO_y sample produced by sol–gel drop-casting and annealing at 200 °C along with the fitting resulting from linear combination of reference MoO_3 and MoO_2 as indicated. (c) XRD diagrams of the MoO_y samples produced by sol–gel drop-casting and annealing at 200 (bottom), 400 (middle) and 600 °C (top).

3. Results and discussion

3.1. Intermediate MoO_y films

Fig. 2 shows a comparison of the surface morphology of the MoO_y films obtained after drop casting the MoO_y precursor sols and annealing at 200 (a, d), 400 (b, e) and 600 °C (c, f). The film obtained at 200 °C shows a porous structure with circular pores at different strata as derived from the observation of internal pores within the bigger surface pores (see arrow in Fig. 2a). The presence of the multi-layer porosity is confirmed in the cross section image (Fig. 2d), which suggest that pores may result from cavities created by gas evolving species during sol condensation. It can be observed (Fig. 2b) that the increase of the annealing temperature allows forming a film of sub-micrometer size clusters. Consequently, the thickness was reduced due to the reinforced densification leading to occlusion of the pores (see cross section in Fig. 2e) and, plausibly also, to the desorption of additional by-products of the condensation whose desorption is activated at annealing temperatures up to 400 °C. By increasing the annealing temperature to 600 °C, the crystal growth is drastically activated. The derived in-plane arranged rod-like structures observed (Fig. 2c) resemble previously processed stacking molybdenum oxide [40,41]. Note the arrow indicating an incomplete stacking layer on top of the surface standing rod (Fig. 2c). The cross section view clearly illustrates that the resulting surface standing rods reach thicknesses of circa 200 nm. Meanwhile, the surface roughness is very low and comparable to the roughness of the underlying Si substrate (Fig. 2f). These observations confirm thus that the initially porous conformable layer obtained at low temperature condensation transforms into a discontinuous film of thick surface-standing layered islands.

Ellipsometry was used as a fast analytical technique to identify the nature of the coating resulting after the seven cycles of casting-condensation of MoO_y precursor sol. The ellipsometric parameters ψ and Δ for the $MoO_y/SiO_2/Si$ stack annealed at 600 °C are shown in Fig. 3 (a). The experimental data were compared with a model based on a polycrystalline MoO_3 thin film deposited onto SiO_2/Si substrate. The agreement between the model and the data is a first good indicator that the synthesized oxide is MoO_3.

In order to deepen our knowledge in the properties of the low temperature processed MoO_y film, a XAS experiment was conducted at the Mo K edge. The XAS spectrum of the sample annealed at 200 °C is shown in Fig. 3b. In the region close to the absorption edge one can distinguish a small ankle at an energy below 20,050 eV, which has been identified through reversible bulk reduction and oxidation processes with a MoO_3 phase [42]. However, the absence of structure at the adsorption edge maximum above 20,050 eV is characteristic of MoO_2 [42]. This indicates that the sample is at a mixed state between MoO_3 and MoO_2. In fact, the experimental spectrum was simulated (see additional fitting curve) by the linear combination of the spectra associated to reference MoO_3 and MoO_2 (with a circa 85% and 15% contribution, respectively, as illustrated in Fig. 3b). Additionally, it was not possible to obtain information from the fine structure oscillations due to the high noise/oscillation-signal ratio, which is most probably influenced by the fluorescence measurement mode and the low degree of crystallinity/order of the sample itself. Thus, the data suggest that the MoO_y films condensed at low temperature are poorly condensed and in an undetermined oxidation state, which can be induced by the presence of carbonyl byproducts of the xerogel formation reaction.

The X-ray diffractograms of MoOx200, MoOx400 and MoOx600 are shown in Fig. 3c. The bump in the 20–30° 2θ range present in the diffractogram of the sample annealed at 200 °C confirms the absence of long-range order of MoO_y phases, in agreement with the XAS spectrum. Note that the well-defined diffraction peaks observed in this sample (i.e. at circa 39, 45 and 56 °C are related to the substrate). The diffraction peaks of the samples annealed at 400 and 600 °C correspond to orthorhombic α-MoO_3 (Pbnm or group 62, COD 969009670), which is the most stable MoO_3 phase [40,41] with lattice parameters a = 3.96 Å, b = 13.86 Å and c = 3.69 Å. However, the sample annealed at 600 °C presents peaks corresponding to the orthorhombic Mo_4O_{11} suboxide (Pna21 or group 33, COD 961521062), which is activated at high temperature [40]. The morphologic changes observed by SEM upon annealing at 600 °C correlate well with additional changes observed in the diffraction diagram. In fact, the intensity of the (0 4 0) α-MoO_3 peak drastically increases, which suggests that the observed rod structures are oriented with their *b* axis pointing out of the substrate. The considerable decrease of the full width at half maximum (FWHM) of the diffraction peaks also denotes a thermally induced crystallite growth, in agreement with SEM images.

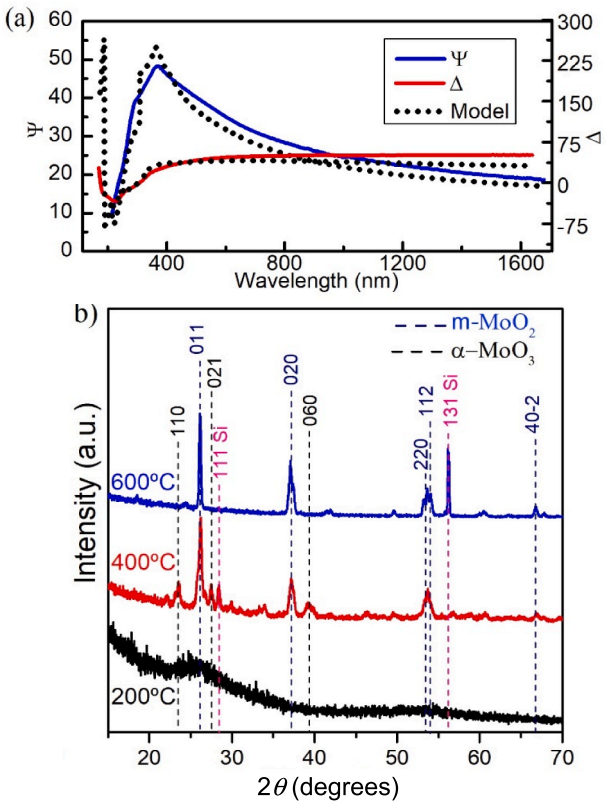

Fig. 4. (a) ψ and Δ dependence with light wavelength as derived from ellipsometry for the $MoO_y/SiO_2/Si$ stack after reduction at 600 °C. (b) XRD diagrams of the MoO_y samples produced by sol–gel drop-casting and annealing at 200 (bottom), 400 (middle) and 600 °C (top) after reduction treatment at the respective annealing temperature.

3.2. Reduction of MoO_y films

Fig. 4 shows the results of characterization of the MoO_y samples after a reduction process. Ellipsometry was used to characterize the sample annealed and reduced at 600 °C. Fig. 4a depicts the behavior of the ellipsometric parameters ψ and Δ for the reduced $MoO_y/SiO_2/Si$ stack. In this case, the oxide used in the model was MoO_2 instead of MoO_3. The good agreement between the data and the model suggests that the reduction process was successful.

The X-Ray diffractograms of the samples reduced at 200, 400 and 600 °C are shown in Fig. 4b. The diffractogram corresponding to the sample reduced at the lowest temperature confirms that there is no activation of a crystallization and no evidence can be extracted from the efficiency of the reduction process at 200 °C. At 400 °C the diffractograms show that, along with peaks corresponding to the starting α-MoO_3 phase, there is a set of additional peaks attributed to monoclinic MoO_2 (P121nc1 or group 14, COD 1548687) which is its most stable phase

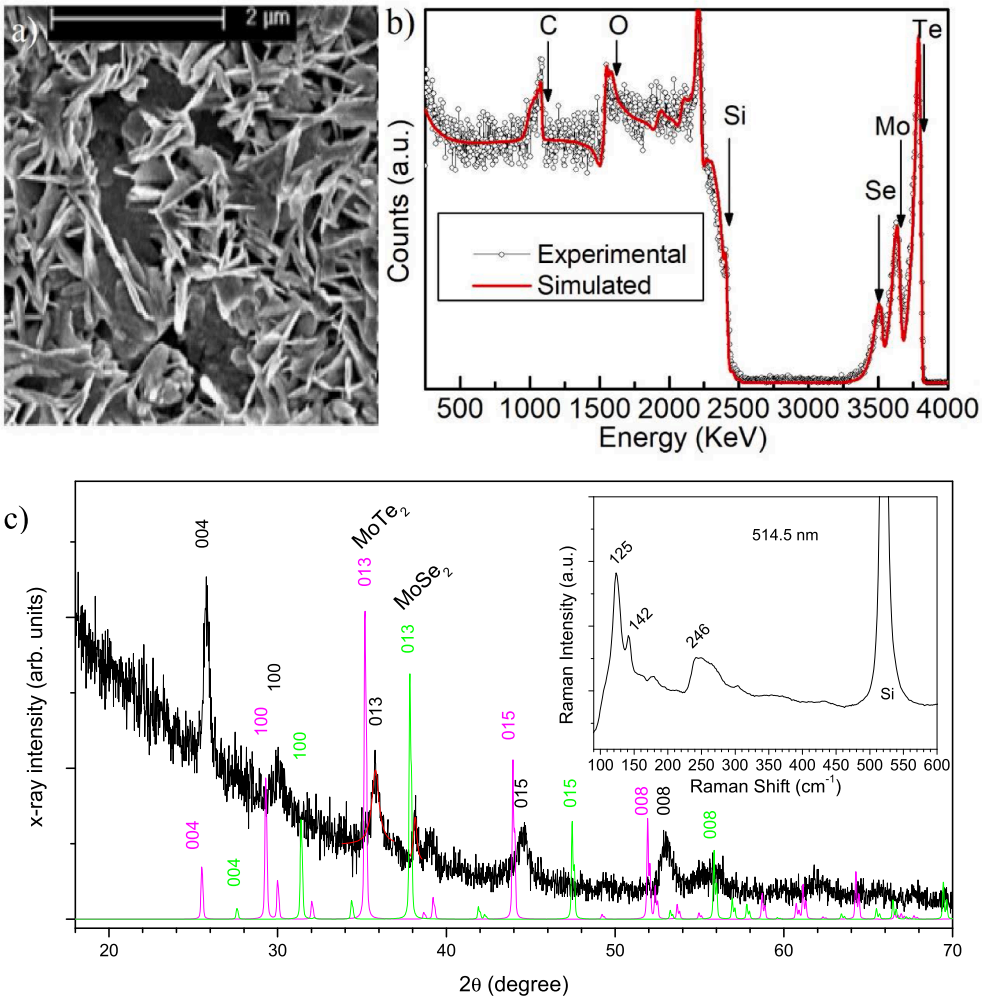

Fig. 5. (a) SEM micrograph from the surface of a $MoTe_2/MoSe_2$ composite film produced by isothermal closed space vapour transformation of the MoO_x film. (b) RBS spectrum of the $MoTe_2/MoSe_2$ composite film. **c)** XRD diagram of the $MoTe_2/MoSe_2$ composite produced at 600 °C, showing the presence of a transformed 2H-$MoTe_2$ (pdf:15–658) with $MoTe_{2(1-x)}Se_{2x}$ structure and 2H-$MoSe_2$ (pdf:29–914). Inset. Mean Raman spectrum obtained at normal incidence from the $MoTe_2/MoSe_2$ composite.

[18,40] and presents lattice parameters a = 5.58 Å, b = 4.84 Å, c = 5.61 Å y β = 120.98°. Therefore, it can be deduced that, although the reduction is considerably activated at 400 °C, it is not complete. However, by increasing the temperature of the reduction process to 600 °C, the diffractogram changes notably with a disappearance of the peaks associated to α-MoO_3 (only peaks related to the substrate appear along the peaks corresponding to m-MoO_2). As in the case of the samples without reduction, the FWHM decrease for samples obtained at the highest reduction temperature confirms a thermally activated increase of the crystallite size.

3.3. Isothermal closed space vapor transformation

Molybdenum oxides are commonly used as precursors for the growth of molybdenum dichalcogenides by exposing the oxide to the chalcogen element vapor. In the present study, in order to illustrate that bi-chalcogen structures can be grown, the chalcogen source was a Te-Se mixture. Fig. 5a shows the SEM image of the sample annealed, reduced and telluro-selenized at 600 °C. This condition was chosen as the optimal from the previous studies for the preparation of a MoO_2 starting layer. A drastic change in the surface morphology is observed with multi-oriented flake-like structures standing off the Si substrate. Relevantly, the density of nucleated structures is drastically increased with respect to the structure of the starting α-MoO_3 film. This observation suggests that the growth, rather than a substitution process, passes through deposition of the chalcogen atoms and consumption of the molybdenum oxide structures.

An RBS study was performed to estimate the stoichiometry of the synthesized TMD (Fig. 5b). The simulation of this spectrum allows determining the composition and average thickness of the deposited structures, leading to the determination of a Te/Se atomic ratio of 3.64 and a Mo/(Te + Se) ratio of 0.54, near the expected stoichiometric MoX_2. The result confirms that for the considered Te:Se atomic ratio of 8:2 (i.e. Te/Se = 4), Se is considerably more efficiently transported and condensed on the film. This effect is produced by the higher vapor pressure of Se as compared to Te during ICSV at 600 °C. Additionally, the RBS experiment performed at C-resonant conditions magnifies the intensity related to the carbon peak and also that associated to oxygen. The spectrum shows that after the processing from sol to TMD, there is still a clear trace of carbonyl-carboxy species, which are known to strongly bond to TMO structures.

An XRD study confirmed the polycrystalline structure of the processed TMD. The main peaks in the diffractograms plotted in Fig. 5c were indexed according to the reference data for hexagonal (P63/mmc symmetry group) $MoTe_2$ and $MoSe_2$ with pdf numbers 15–658 and 29–914, respectively. Two main observations can be derived from the results. Firstly, the diffractogram shows no peaks of pure Se or Te, suggesting that the temperatures and reaction times were well adapted to the processing of a TMD composite or solid solution. Secondly, the presence of a solid solution derived from Se substituted $MoTe_2$ is confirmed by the shifted diffraction peaks of hexagonal 2H-$MoTe_2$. This solution consists of a pure $MoTe_{2(1-x)}Se_{2x}$ hexagonal phase (a mix of 2H-$MoTe_2$ and 2H-$MoSe_2$) with no traces of the distorted octahedral (1T′) phase as indicated by the absence of splitting in the (00L) peaks [43–45].

The peaks in our sample are slightly shifted to higher 2θ values with respect to the 2H-$MoTe_2$ reference positions. In fact, since lattice parameters of $MoSe_2$ (a/c = 0.3288/1.2900 nm) are smaller than those of $MoTe_2$ (a/c = 0.3519/1.3964 nm), such shift is explained by assuming the formation of a $MoTe_{2(1-x)}Se_{2x}$ alloy phase. Using the Vegard Law for the interplanar distances of the observed planes, ($d_{MoTe2(1-x)Se2x} = (1-x)d_{MoTe2} + xd_{MoSe2}$) we obtained an average molar fraction (x) of $MoSe_2$ of 0.25, which means a $MoTe_{1.5}Se_{0.5}$ alloy. This represents a Te/Se relation of 3.0 in relatively good agreement with the RBS result (0.275), although denoting some missing phase accounting for more Se. In fact, the XRD diagram of Fig. 5.c, presents a peak at 38° denoting the presence of some 2H-$MoSe_2$ crystals. A phase refinement based in lorentzian fitting of the (0 1 3) peaks corresponding to the two hexagonal phases resulted in an estimation of a 14.8% for the 2H-$MoSe_2$ phase. Finally, it is observed that there is a preferential growth of $MoTe_{2(1-x)}Se_{2x}$ along the (0 0 1) direction. This growth has been related to the Si (1 0 0) plane in other similar works [43,44], but SEM images do not allow to establish such relationship in the current investigation. The main difference between those works and the present one is that the precursor MoO_y had been synthesized by sputtering [43] and by CVD [44].

The inset to Fig. 5c shows the averaged Raman spectrum taken from nine different points on the sample surface and reflects a combination of the spectra of film and substrate. In fact, the strong peak at 520 cm^{-1} corresponds to the one-phonon peak of crystalline silicon and the weak feature at 300 cm^{-1} is a silicon second order Raman band [46]. The other peaks of the Raman spectrum originate from the film. The wide band around 250 cm^{-1} corresponds to the E^1_{1g} phonon mode of 2H-$MoTe_2$ and the effect of alloying with $MoSe_2$ [47].

The peak at 125 cm^{-1} corresponds to the E_{1g} phonon of 2H-$MoTe_2$ [48]. This peak appears only for backscattering on the edge of the layers [48], as would occur for flakes oriented normal to the substrate. The peak at 142 cm^{-1} could be a second order mode [49] activated by the substitution of Te atoms by Se. Alternative explanations based on the presence of pure Te phases [50] or degraded 1T'-$MoTe_2$ [51] do not agree with the XRD analysis of the present $MoTe_2$/$MoSe_2$ composites. Overall, Raman analysis suggests that the 2H-$MoTe_2$ layers are oriented perpendicular to the substrate, which is in agreement with SEM observations.

4. Conclusions

The present work demonstrates that the sol–gel process can be used to condensate MoO_3 from an isopropoxide precursor at low temperatures of 200 °C. The films formed by sol casting can be further processed by thermal reduction in Ar:H_2 at 600 °C to obtain conformal in-plane-ordered MoO_2 islands. Such films have been used to produce $MoTe_2$/$MoSe_2$ composite films by isothermal closed space vapour tellurosselenization at 600 °C. The process parameters adapt well to the formation of $MoTe_2$/$MoSe_2$ dichalcogenide phases, with no trace of pure Se or Te. The Te rich phase corresponds rather to a hexagonal $MoTe_{2(1-x)}Se_{2x}$ pseudo binary alloy, being x close to 0.25. The Se rich phase represents approximately a 15% of the total $MoTe_2$/$MoSe_2$ composite. In contrast with the structure of the starting MoO_2 phase, these films show a flaky structure with flakes standing out-of-plane, as supported by morphological observations and Raman scattering. This suggests that the films grow by consumption of the previously nucleated MoO_2 crystals, rather than by a soft exchange of oxygen by the chalcogen atoms. This further suggests a strong interaction of the flakes with the substrate since dangling bonds on the edge of 2D materials are highly reactive leading to covalent bonding with affine structures.

The abundance of out-of plane TMD crystals suggests the presence of a high porosity and a large surface area, ideal for ion or gas exchange, which is extremely attractive for the processing of sensing and catalytic devices.

CRediT authorship contribution statement

A. Fernandez García: Investigation, Writing - original draft. **V. Torres-Costa:** Data curation, Writing - review & editing. **O de Melo:** Methodology, Writing - review & editing. **F. Agulló Rueda:** Investigation, Writing - review & editing. **G.R. Castro:** Investigation, Data curation, Writing - review & editing. **M. Manso Silvan:** Conceptualization, Investigation, Writing - review & editing.

Declaration of Competing Interest

The authors declare that they have no known competing financial interests or personal relationships that could have appeared to influence the work reported in this paper.

Acknowledgements

Authors thank Luis García Pelayo for his technical assistance during materials processing. XAS experiments performed at the BM25A Spanish line at the ESRF were granted through allocation 25-01-1088. The current research was funded by grant CTQ2017-84309-C2-2-R from Ministerio de Ciencia e Innovación (Spain). The authors acknowledge the ESRF and the Ministerio de Ciencia, Innovación y Universidades (Spain), for provision of synchrotron radiation facilities and the Consejo Superior de Investigaciones Científicas (Spain) financial support for the operation of the beamline under Grant No. PIE 2010 6 OE 013.

References

[1] Q.L. Zhao, Z.J. Xie, Y.P. Peng, K.Y. Wang, H.D. Wang, X.N. Li, H.W. Wang, J. S. Chen, H. Zhang, X.B. Yan, Current status and prospects of memristors based on novel 2D materials, Mater. Horiz. 7 (2020) 1495–1518.
[2] F. Li, T. Shen, C. Wang, Y.P. Zhang, J.J. Qi, H. Zhang, Recent advances in strain-induced piezoelectric and piezoresistive effect-engineered 2D semiconductors for adaptive electronics and optoelectronics, Nano-Micro Letters 12 (2020), 106.
[3] B. Wang, S.P. Zhong, Y.Q. Ge, H.D. Wang, X.L. Luo, H. Zhang, Present advances and perspectives of broadband photo-detectors based on emerging 2D-Xenes beyond graphene, Nano Res. 13 (2020) 891–918.
[4] D.Z. Zhang, Z.M. Yang, S.J. Yu, Q. Mi, Q.N. Pan, Diversiform metal oxide-based hybrid nanostructures for gas sensing with versatile prospects, Coord. Chem. Rev. 413 (2020), 213272.
[5] S.G. Yuan, S.Y. Pang, J.H. Hao, 2D transition metal dichalcogenides, carbides, nitrides, and their applications in supercapacitors and electrocatalytic hydrogen evolution reaction, Appl. Phys. Rev. 7 (2020), 021304.
[6] R.K. Jha, N. Bhat, Recent progress in chemiresistive gas sensing technology based on molybdenum and tungsten chalcogenide nanostructures, Adv. Mater. Interfaces 7 (2020), 1901992.
[7] B.Y. Ren, Y.C. Wang, J.Z. Ou, Engineering two-dimensional metal oxides via surface functionalization for biological applications, J. Mater. Chem. B 8 (2020) 1108–1127.
[8] G.P. Neupane, L.L. Zhang, T. Yildirim, K. Zhou, B.W. Wang, Y.L. Tang, W.D. Ma, Y. Z. Xue, Y.R. Lu, A prospective future towards bio/medical technology and bioelectronics based on 2D vdWs heterostructures, Nano Res. 13 (2020) 1–17.
[9] M.A. Cazalilla, H. Ochoa, F. Guinea, Quantum spin hall effect in two-dimensional crystals of transition-metal dichalcogenides, Phys. Rev. Lett. 113 (2014), 077201.
[10] D.H. Keum, S. Cho, J.H. Kim, D.H. Choe, H.J. Sung, M. Kan, H. Kang, J.Y. Hwang, S.W. Kim, H. Yang, K.J. Chang, Y.H. Lee, Bandgap opening in few-layered monoclinic MoTe2, Nat. Phys. 11 (2015), 482–U144.
[11] L. Wang, I. Gutierrez-Lezama, C. Barreteau, N. Ubrig, E. Giannini, A.F. Morpurgo, Tuning magnetotransport in a compensated semimetal at the atomic scale, Nat. Commun. 6 (2015), 8892.
[12] P.K. Chow, R.B. Jacobs-Gedrim, J. Gao, T.M. Lu, B. Yu, H. Terrones, N. Koratkar, Defect-induced photoluminescence in mono layer semiconducting transition metal dichalcogenides, ACS Nano 9 (2015) 1520–1527.
[13] A.R. Klots, A.K.M. Newaz, B. Wang, D. Prasai, H. Krzyzanowska, J.H. Lin, D. Caudel, N.J. Ghimire, J. Yan, B.L. Ivanov, K.A. Velizhanin, A. Burger, D. G. Mandrus, N.H. Tolk, S.T. Pantelides, K.I. Bolotin, Probing excitonic states in suspended two-dimensional semiconductors by photocurrent spectroscopy, Sci. Rep. 4 (2014), 6608.
[14] P. Rivera, J.R. Schaibley, A.M. Jones, J.S. Ross, S.F. Wu, G. Aivazian, P. Klement, K. Seyler, G. Clark, N.J. Ghimire, J.Q. Yan, D.G. Mandrus, W. Yao, X.D. Xu, Observation of long-lived interlayer excitons in monolayer MoSe2-WSe2 heterostructures, Nat. Commun. 6 (2015), 6242.
[15] G. Wang, L. Bouet, D. Lagarde, M. Vidal, A. Balocchi, T. Amand, X. Marie, B. Urbaszek, Valley dynamics probed through charged and neutral exciton emission in monolayer WSe2, Phys. Rev. B 90 (2014), 075413.

[16] O. Lopez-Sanchez, E. Alarcon Llado, V. Koman, A.F.I. Morral, A. Radenovic, A. Kis, Light generation and harvesting in a van der Waals heterostructure, ACS Nano 8 (2014) 3042–3048.
[17] D.H. Choe, H.J. Sung, K.J. Chang, Understanding topological phase transition in monolayer transition metal dichalcogenides, Phys. Rev. B 93 (2016), 125109.
[18] O. de Melo, L. Garcia-Pelayo, Y. Gonzalez, O. Concepcion, M. Manso-Silvan, R. Lopez-Nebreda, J.L. Pau, J.C. Gonzalez, A. Climent-Font, V. Torres-Costa, Chemically driven isothermal closed space vapor transport of MoO2: thin films, flakes and in situ tellurization, J. Mater. Chem. C 6 (2018) 6799–6807.
[19] L. Britnell, R.M. Ribeiro, A. Eckmann, R. Jalil, B.D. Belle, A. Mishchenko, Y.J. Kim, R.V. Gorbachev, T. Georgiou, S.V. Morozov, A.N. Grigorenko, A.K. Geim, C. Casiraghi, A.H. Castro Neto, K.S. Novoselov, Strong light-matter interactions in heterostructures of atomically thin films, Science 340 (2013) 1311–1314.
[20] D.S. Inosov, V.B. Zabolotnyy, D.V. Evtushinsky, A.A. Kordyuk, B. Buchner, R. Follath, H. Berger, S.V. Borisenko, Fermi surface nesting in several transition metal dichalcogenides, New J. Phys. 10 (2008), 125027.
[21] Q.Y. He, Z.Y. Lin, M.N. Ding, A.X. Yin, U. Halim, C. Wang, Y. Liu, H.C. Cheng, Y. Huang, X.F. Duan, In situ probing molecular intercalation in two-dimensional layered semiconductors, Nano Lett. 19 (2019) 6819–6826.
[22] H. Pan, Y.W. Zhang, Tuning the electronic and magnetic properties of MoS2 nanoribbons by strain engineering, J. Phys. Chem. C 116 (2012) 11752–11757.
[23] Y.D. Zhang, Z.S. Meng, Q. Shi, H.Q. Gao, Y.Z. Liu, Y.H. Wang, D.W. Rao, K. M. Deng, R.F. Lu, Nanoporous MoS2 monolayer as a promising membrane for purifying hydrogen and enriching methane, J. Phys.-Condensed Matter 29 (2017), 375201.
[24] M.H. Johari, M.S. Sirat, M.A. Mohamed, S. Nasir, M.A.M. Teridi, A.R. Mohmad, Effects of Mo vapor concentration on the morphology of vertically standing MoS2 nanoflakes, Nanotechnology 31 (2020), 305710.
[25] X.S. Chen, Z.G. Wang, Y.F. Qiu, J. Zhang, G.B. Liu, W. Zheng, W. Feng, W.W. Cao, P.A. Hu, W.P. Hu, Controlled growth of vertical 3D MoS2(1–x)Se2x nanosheets for an efficient and stable hydrogen evolution reaction, J. Mater. Chem. A 4 (2016) 18060–18066.
[26] M.A. Islam, J. Church, C. Han, H.S. Chung, E. Ji, J.H. Kim, N. Choudhary, G.H. Lee, W.H. Lee, Y. Jung, Noble metal-coated MoS2 nanofilms with vertically-aligned 2D layers for visible light-driven photocatalytic degradation of emerging water contaminants, Sci. Rep. 7 (2017), 14944.
[27] J. Gao, L. Li, J.W. Tan, H. Sun, B.C. Li, J.C. Idrobo, C.V. Singh, T.M. Lu, N. Koratkar, Vertically oriented arrays of ReS2 nanosheets for electrochemical energy storage and electrocatalysis, Nano Lett. 16 (2016) 3780–3787.
[28] P.P. Kang, H.Y. Nan, X.M. Zhang, H.X. Mo, Z.H. Ni, X.F. Gu, K. Ostrikov, S.Q. Xiao, Controllable synthesis of crystalline ReS2(1–x)Se2x monolayers on amorphous sio2/si substrates with fast photoresponse, Adv. Opt. Mater. 8 (2020), 1901415.
[29] W.F. Yang, H. Kawai, M. Bosman, B.S. Tang, J.W. Chai, W.L. Tay, J. Yang, H. L. Seng, H.L. Zhu, H. Gong, H.F. Liu, K.E.J. Goh, S.J. Wang, D.Z. Chi, Interlayer interactions in 2D WS2/MoS2 heterostructures monolithically grown by in situ physical vapor deposition, Nanoscale 10 (2018) 22927–22936.
[30] C. Martella, L. Ortolani, E. Cianci, A. Lamperti, V. Morandi, A. Molle, Large-area patterning of substrate-conformal MoS2 nano-trenches, Nano Res. 12 (2019) 1851–1854.
[31] P.M. Campbell, C.J. Perini, J. Chiu, A. Gupta, H.S. Ray, H. Chen, K. Wenzel, E. Snyder, B.K. Wagner, J. Ready, E.M. Vogel, Plasma-assisted synthesis of MoS2, 2d Materials 5 (2018) 12.
[32] M.A. Sriram, P.N. Kumta, The thio-sol-gel synthesis of titanium disulfide and niobium disulfide Part 1. - Materials chemistry, J. Mater. Chem. 8 (1998) 2441–2451.
[33] M.V. Nardi, M. Timpel, G. Ligorio, N.Z. Morales, A. Chiappini, T. Toccoli, R. Verucchi, R. Ceccato, L. Pasquali, E.J.W. List-Kratochvil, A. Quaranta, S. Dire, Versatile and scalable strategy to grow sol-gel derived 2H-MoS2 thin films with superior electronic properties: a memristive case, ACS Appl. Mater. Interfaces 10 (2018) 34392–34400.
[34] L. Fan, Suni II, Electrodeposition and capacitance measurements of WS2 thin films, J. Electrochem. Soc. 164 (2017) D681–D686.
[35] P.K. Rastogi, S. Sarkar, D. Mandler, Ionic strength induced electrodeposition of two-dimensional layered MoS2 nanosheets, Appl. Mater. Today 8 (2017) 44–53.
[36] M. Langlet, P. Jenouvrier, A. Kim, M. Manso, M.T. Valdez, Functionality of aerosol-gel deposited TiO2 thin films processed at low temperature, J. Sol-Gel Sci. Technol. 26 (2003) 759–763.
[37] J.H. Harreld, W. Dong, B. Dunn, Ambient pressure synthesis of aerogel-like vanadium oxide and molybdenum oxide, Mater. Res. Bull. 33 (1998) 561–567.
[38] H. Takahashi, T. Akiba, K. Imura, T. Shiino, K. Deguchi, N.K. Sato, H. Sakai, M. S. Bahramy, S. Ishiwata, Anticorrelation between polar lattice instability and superconductivity in the Weyl semimetal candidate MoTe2, Phys. Rev. B 95 (2017), 100501.
[39] M. Mayer, SIMNRA, a simulation program for the analysis of NRA, RBS and ERDA, Appl. Acceler. Res. Ind., Pts 1 and 2 (475) (1999) 541–544.
[40] I.A. de Castro, R.S. Datta, J.Z. Ou, A. Castellanos-Gomez, S. Sriram, T. Daeneke, K. Kalantar-zadeh, Molybdenum oxides - from fundamentals to functionality, Adv. Mater. 29 (2017), 1701619.
[41] V. Kumar, A. Sumboja, J.X. Wang, V. Bhavanasi, V.C. Nguyen, P.S. Lee, Topotactic phase transformation of hexagonal MoO3 to layered MoO3-II and its two-dimensional (2D) nanosheets, Chem. Mater. 26 (2014) 5533–5539.
[42] T. Ressler, J. Wienold, R.E. Jentoft, T. Neisius, Bulk structural investigation of the reduction of MoO3 with propene and the oxidation of MoO2 with oxygen, J. Catal. 210 (2002) 67–83.
[43] E. Sanchez-Montejo, G. Santana, A. Dominguez, L. Huerta, L. Hamui, M. Lopez-Lopez, H. Limborco, F.M. Matinaga, M.I.N. da Silva, A.G. de Oliveira, J. C. Gonzalez, O. de Melo, Phase stability in MoTe2 prepared by low temperature Mo tellurization using close space isothermal Te annealing, Mater. Chem. Phys. 198 (2017) 317–323.
[44] X.S. Xu, X.B. Li, K.Q. Liu, J. Li, Q.L. Feng, L. Zhou, F.F. Cui, X. Liang, Z.B. Lei, Z. H. Liu, H. Xu, Thermodynamics and kinetics synergetic phase-engineering of chemical vapor deposition grown single crystal MoTe2 nanosheets, Cryst. Growth Des. 18 (2018) 2844–2850.
[45] K. Ueno, K. Fukushima, Changes in structure and chemical composition of alpha-MoTe2 and beta-MoTe2 during heating in vacuum conditions, Appl. Phys Express 8 (2015), 095201.
[46] W.P. Acker, B. Yip, D.H. Leach, R.K. Chang, The use of a charge-coupled device and position-sensitive resistive anode detector for multiorder spontaneous Raman-spectroscopy from silicon, J. Appl. Phys. 64 (1988) 2263–2270.
[47] T.J. Wieting, A. Grisel, F. Levy, Interlayer bonding and localized charge in mose2 and alpha-mote2, Physica B & C 99 (1980) 337–342.
[48] S. Caramazza, A. Collina, E. Stellino, F. Ripanti, P. Dore, P. Postorino, First- and second-order Raman scattering from MoTe2 single crystal, Eur. Phys. J. B 91 (2018), 35.
[49] H.H. Guo, T. Yang, M. Yamamoto, L. Zhou, R. Ishikawa, K. Ueno, K. Tsukagoshi, Z. D. Zhang, M.S. Dresselhaus, R. Saito, Double resonance Raman modes in monolayer and few-layer MoTe2, Phys. Rev. B 91 (2015), 205415.
[50] N.V. Sochinskii, M.D. Serrano, E. Dieguez, F. Agullorueda, U. Pal, J. Piqueras, P. Fernandez, Effect of thermal annealing on te precipitates in cdte wafers studied by Raman-scattering and cathodoluminescence, J. Appl. Phys. 77 (1995) 2806–2808.
[51] S.-Y. Chen, C.H. Naylor, T. Goldstein, A.T.C. Johnson, J. Yan, Intrinsic phonon bands in high-quality monolayer T ' molybdenum ditelluride, ACS Nano 11 (2017) 814–820.